Cross-Medium Networking With Transflective Flexible Metasurfaces

Ruichun Ma, *Member, IEEE*, and Wenjun Hu, *Member, IEEE*

***Abstract*—Emerging wireless networks increasingly venture beyond over-the-air communication, such as deep-tissue networking for medical sensors, air-water communication for oceanography, and soil sensing for agriculture. They face the fundamental challenge of significant reflection and power loss at medium interfaces. We present RF-Mediator, a transflective metasurface placed near a medium interface to program the behavior of the physical boundary. Our hardware design comprises a single layer of varactor-based surface elements with specific metallic patterns and wiring. With the biasing voltage tuned element-wise, the surface dynamically mediates between the adjacent media to control and utilize both signal reflection and transmission, enhancing connectivity for wireless endpoints on both sides. A multi-stage control algorithm efficiently determines the surface configuration to handle dynamic adaptation needs for joint medium impedance matching and beamforming towards multiple endpoints simultaneously. We implement a lightweight and flexible metasurface prototype and experiment with diverse cross-medium setups. Extensive evaluation shows that RF-Mediator provides a median power gain of 8 dB for air-tissue links, reaching up to 30 dB gain for backscatter links, and up to 18 dB for multiple links concurrently.**

***Index Terms*—Wireless networking, cross-medium, metasurfaces, reconfigurable intelligent surfaces, impedance matching.**

I. Introduction

WIRELESS networking applications increasingly involve communication media not limited to air only. The signals may need to cross over medium boundaries, especially air-tissue interfaces [2], [3], [4], [5], [6], [7], air-water interfaces [8], [9], and air-ground interfaces [10], [11]. Air-tissue networking is a key enabler for numerous *in-vivo* medical applications, such as vital sign monitoring [12], [13], wireless gastrointestinal diagnosis [14], [15], on-demand drug delivery [16], and untethered neuro-stimulation therapy [17], [18]. Air-water networking supports underwater IoT applications including aquaculture [19], environmental sensing [20], and monitoring submerged infrastructure [21]. Air-ground networking is useful for underground operations [22], [23] and soil sensing applications [10], [24].

Cross-medium networking, however, is much more challenging than its over-the-air counterpart (Section II). When two adjacent media exhibit different propagation characteristics, some signal power is reflected back by the medium interface rather than crossing the interface (Figure 1). Such reflection can be substantial, e.g., around 90% of the signal power is reflected for air-to-tissue links on 2.4 GHz (Figure 2), reducing the through-interface signal power by 10 dB and creating strong, unwanted reflections. This happens in both directions, i.e., whether air-to-tissue or tissue-to-air, which is especially significant for backscatter devices with low transmission power to start with. Strong reflections can further cause severe self-interference and multipath fading.

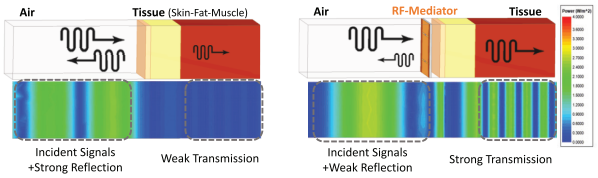

(a) Without RF-Mediator (b) With RF-Mediator

Fig. 1. RF-Mediator matches the impedance of adjacent media for wave propagation (left-to-right). The heat maps show signal power distributions.

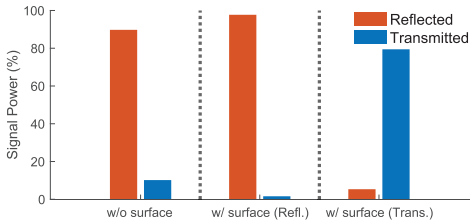

Fig. 2. Reflected and transmitted-through power percentages at air-body interface. With the metasurface deployed, we can control the power percentages with different surface states.

Most existing solutions operate at the communication endpoints, boosting the transmitted or received power via some form of beamforming [3], [5], [6] or moving the endpoints to the interface [25], [26], [27]. While these *compensate for* the power loss at the interface or *avoid* crossing the interface, they cannot address the root cause of the cross-medium challenge, thus leading to side effects (Section II-B).

Fundamentally, medium permittivity differences cause impedance mismatch at the interface (Section II-A). If we consider propagation media as transmission lines for signals, conceptually, we can place an RF component to counter the impedance mismatch at the medium interface. Note, however, that we target dynamic environments instead of highly controlled circuit boards, a perspective shift from conventional impedance control [28].

Received 7 July 2024; revised 2 June 2025; accepted 12 June 2025; approved by IEEE TRANSACTIONS ON NETWORKING Editor H. Hassanieh. Date of publication 10 July 2025; date of current version 18 December 2025. *(Corresponding author: Ruichun Ma.)*

Ruichun Ma is with Microsoft Research Asia, Vancouver, BC V7Y 1G5, Canada (e-mail: ruichunma@microsoft.com).

Wenjun Hu is with ECE Department, Yale University, New Haven, CT 06520 USA (e-mail: wenjun.hu@cantab.net).

Digital Object Identifier 10.1109/TON.2025.3584675

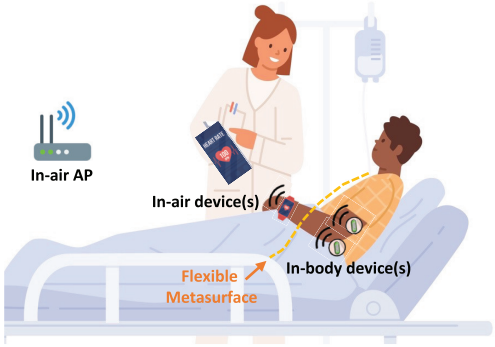

Fig. 3. Illustration of deploying metasurface on a blanket to simultaneously enhance multiple wireless endpoints near the air-body interface for medical monitoring.

Acting as an impedance boundary, a smart surface is well suited to the role of impedance matching between media, the simplest of which is an array of antenna-like metallic elements or patterns. There has been significant interest in augmenting or programming the radio propagation environment with smart surfaces (e.g., [29], [30], [31], [32], [33], [34], [35], [36], [37], [38], [39], [40], [41]) by controlling the signal propagation behavior to improve the endpoint-perceived channel conditions. However, these designs for over-the-air propagation cannot alter the unfavorable propagation behavior when crossing a medium interface. Further, their beamforming capability may degrade due to coupling with a closeby non-air medium. Recent proposals have made head way designing multi-layer metasurfaces for cross-medium reflection mitigation [42], [43]. However, these are one-off, *non-programmable* hardware designs far from handling real-world medium dynamics and wireless channel fluctuations. Further, these designs forego the beamforming gain in previous endpoint-centric solutions, which can be significant in our experiments. Practically, thick, rigid circuit boards are ill-suited for deployment.

Instead, we present RF-Mediator, a transflective and flexible metasurface system that programs the medium interface (Section III). By dynamically mediating the impedance difference of adjacent media, the surface interacts with the physical medium boundary nearby without direct contact and alters the interface's behavior. When tuned to an appropriate surface admittance/impedance, RF-Mediator significantly boosts the through-interface transmission power of cross-medium links. Figure 1 shows the signal power distributions at an air-tissue interface with and without our surface. Different surface configurations control the proportion of signal reflection and transmission through the interface. Therefore, the same metasurface can both reflect the signal power and boost signal transmission, i.e., being transflective (Figure 2). RF-Mediator further performs beamforming with element-wise control. With joint medium impedance matching and beamforming, we can boost the received signal strength for multiple endpoints on either side of the interface using through-interface transmission and reflection respectively.

The design for RF-Mediator addresses several challenges. First, we need a hardware design that can achieve dynamic medium impedance matching and beamforming. Our surface hardware comprises carefully designed metallic patterns, interconnected with varactor diodes, and individually controlled biasing voltage wires. Adjusting the varactor biasing voltages produces a tunable surface admittance range specific for our purpose; The element-wise on-off control effect achieves an additional beamforming gain (Section III-C). Second, we need an efficient control algorithm for impedance matching under environmental dynamics, such as different medium compositions, varying surface-medium gaps, and fluctuating multipath channel conditions. Supporting multiple endpoints on both sides of the surface concurrently further requires joint optimization of both the through-interface and reflected power. Our multi-stage algorithm caters to all needs at once, by successively performing surface-wide coarse-grained impedance matching, then element-wise beamforming, and finally fine-grained voltage adjustment (Section III-D). Third, practically, the surface needs to be lightweight and adaptable to medium interface shapes across diverse application scenarios. Our low-complexity single-layer design allows implementation as flexible and conformal prototypes.

We fabricated RF-Mediator prototypes on a thin, flexible PCB substrate (Section IV, Figure 11). The design's simplicity and flexibility enables integration into various form factors. For air-tissue networking, the surfaces can be incorporated in blankets or garments like hospital gowns for medical purposes (Figure 3). For air-water networking, the surfaces can mimic floating aquatic plant leaves, bridging on-land gateways and underwater IoT devices. For air-soil networking, the surfaces may take the form of agricultural mulch films, assisting drones with data collection from underground sensors [44].

Extensive experimental evaluation (Section V) shows RF-Mediator reduces the reflection at air-water and air-tissue interfaces by over 10 dB, confirming adequate medium impedance matching. We achieve a median throughput increase of 55% and up to $4\times$ for air-water Wi-Fi links, which can facilitate demanding applications like image or video transmission [15], [20]. For (emulated) in-water backscatter links, our system provides a median received power gain of 10 dB and up to 30 dB. When enhancing multiple links simultaneously, RF-Mediator shows a median power gain of 6 dB and up to 18 dB for two in-tissue devices using *one* shared surface configuration. Given its transflective nature, the surface hardware also provides up to 8 dB gain for in-air links by using the reflection, without compromising the through-interface air-tissue link enhancement. Moreover, RF-Mediator's programmability ensures robust performance despite variations in medium consistency (tissue fat thickness), surface-medium gaps, channel conditions, and surface-endpoint distances. Lastly, we highlight the necessity of surface flexibility and the performance of a bent surface with simulations (Figure 28).

In summary, this paper makes the following contributions. First, we highlight a new signal manipulation modality, i.e., dynamic impedance matching of adjacent media, and identify the knobs for programmability to support cross-medium wireless networking. We also show the importance of further incorporating beamforming. Second, we propose the first electronically programmable metasurface design for cross-medium networking, with a focus on air-tissue networking as a demanding scenario. Together with an efficient, multi-stage control algorithm, our design constitutes a novel end-to-end

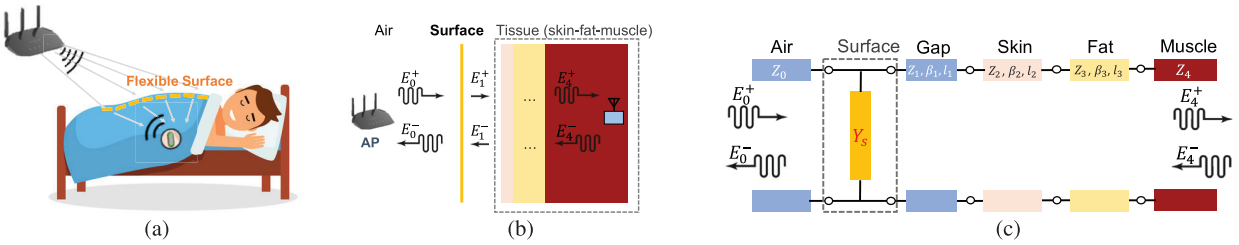

Fig. 4. Surface operation illustration. **(a)** Air-to-tissue application example: An AP connects to an in-body (backscatter) endpoint through a metasurface for long-term medical monitoring. **(b)** Analytical model of the metasurface and tissue layers. **(c)** Microwave circuit model. We use a cascaded two-port (circles in the figure) microwave network to model signal propagation, deriving the desired *surface admittance* (Y_s) to minimize the reflection, E_0^-, and boost the through-interface transmission, E_4^+.

system. It dynamically controls signal propagation (reflection and transmission) and beamforming at medium interfaces to enhance multiple links at once as a shared infrastructure. Third, we present a lightweight and flexible metasurface implementation that facilitates practical deployment. Experiments confirm that we can effectively program the physical medium boundary behavior for significant link enhancement and throughput increase with RF-Mediator.

II. Background and Motivation

We first explain RF signal propagation behavior across any medium interface. Then we summarize existing cross-medium solutions and their shortcomings to motivate our design.

A. Signal Propagation at Medium Interfaces

Transmission and reflection. We characterize a medium with two parameters: *relative permittivity* ϵ_r and *relative permeability* μ_r, which describe wave propagation relative to vacuum. The intrinsic wave impedance of the medium, denoted as $Z = \frac{\sqrt{\mu_r}}{\sqrt{\epsilon_r}} Z_0$ (with $Z_0 = 376.7\Omega$ representing the vacuum impedance), captures the electric-to-magnetic field strength ratio [45]. Given that μ_r is unitary for typical media of interest, the medium impedance is primarily governed by the *permittivity*, ϵ_r.

Suppose signals travel from air (relative permittivity $\epsilon_0 = 1$, impedance Z_0) to another medium of interest (ϵ_r, Z_r). Solving the boundary conditions at the interface [45] gives

$$\Gamma = \frac{Z_r - Z_0}{Z_r + Z_0} = \frac{\sqrt{\epsilon_0} - \sqrt{\epsilon_r}}{\sqrt{\epsilon_0} + \sqrt{\epsilon_r}}$$
$$T = 1 + \Gamma = \frac{2Z_r}{Z_r + Z_0} = \frac{2\sqrt{\epsilon_0}}{\sqrt{\epsilon_0} + \sqrt{\epsilon_r}} \quad (1)$$

where Γ and T are the reflection and transmission coefficients of the interface respectively. When the impedance values of adjacent media are not equal or matched, some signal power is reflected at the interface instead of propagating to the other medium. The through-interface power is $\frac{Z_0}{Z_r}|T|^2$, while the power reflected from the interface is $|\Gamma|^2$. Such power loss at the interface happens in both propagation directions.

Table I lists the parameters of several media measured in controlled lab settings [42], [46], [47], and Figure 2 shows the propagation behavior through medium pairs simulated with these parameters in HFSS. Notably, water and tissue (skin, fat, muscle) exhibit higher permittivity, resulting in pronounced reflection and weak transmission at air-water and air-tissue interfaces. Tissue comprises several layers, including skin, fat, and muscle, non-uniform in thickness, leading to multiple reflections before signals reach an in-vivo endpoint. While the exact permittivity values vary slightly in practice depending on the specific medium composition and measurement method, the overall propagation behavior remains the same.

TABLE I
Intrinsic Impedance of Medium, Determined by Permittivity, Causes Impedance Mismatch Between Media

Medium	Air	Water	Skin	Fat	Muscle
Permittivity	1	81	43.75	5.46	55.03
Impedance (Ω)	376.7	41.86	57.0	161.2	50.8

Attenuation and refraction. Common media, like tissue and water, can have high *conductivity*, adding an imaginary part to make permittivity complex-valued and causing notable signal attenuation. For the media considered in this paper, however, their conductivity values are within the range that does not affect the medium impedance significantly. Another phenomenon at the medium interface is signal refraction, which changes the propagation direction. This contributes to multipath fading of through-interface signals. Attenuation and refraction weaken through-interface signal power but do not affect medium impedance (mis)match.

Backscatter signals. Backscatter signals, pivotal for battery-less in-vivo communication [2], [3], [4], [5], [6], [7], encounter amplified challenges at medium interfaces due to the signals propagating through these interfaces twice-once outbound and once inbound. For example, air-tissue backscatter links require the in-vivo endpoints to harvest enough power and the in-air endpoints to receive backscattered signals at sufficient SINR (signal-to-interference-plus-noise ratio). The former is susceptible to the significant through-interface power loss already discussed. For the latter, the received backscatter signals incur reflection power loss twice, in both directions through the medium boundary. Further, strong reflections at the interface also create *self*-interference, significantly decreasing the received SINR at either endpoint.

Combined effects. Collectively, the propagation mechanisms produce three effects: *strong reflection-induced interference*, *through-interface power loss*, and *more complex multipath fading* inside the second medium. Ideally, solutions for cross-medium link improvement should counter all three issues.

B. Related Work

Existing solutions to support cross-medium links fall into a few categories and are susceptible to various limitations.

Enhancing in-vivo endpoints. One common strategy is to *compensate for through-interface power degradation after the fact* via receiver-side beamforming [3], [6] or more effective in-vivo receiver design [4], [5]. However, after-the-fact compensation is usually not as effective as tackling the root cause. It fails to counter the strong reflection at interfaces, causing power waste and large (self-)interference to nearby endpoints. It is also costly, requiring specialized and synchronized multi-antenna hardware or complex receiver design. MeAnt [48] utilizes piezoelectric mechanical antennas, but supports only low datarate and unidirectional communication.

Placing endpoints at the interface. Alternatively, some endpoints can be moved to the medium interface instead to *avoid traversing an interface*, at the expense of limited usability. For example, specially designed antennas [25], [26], [27] on the skin bring discomfort and inhibit mobility, thus hindering long-term monitoring. Deploying an (active) endpoint at the interface usually demands battery power and precludes reusing existing IoT devices as the signal source.

Adding anti-reflection metasurfaces. Unlike endpoint-based approaches, adding metasurfaces to the medium boundary can fundamentally *minimize reflection*. Existing designs [42], [43], [49], [50], [51], [52], [53], however, target a specific medium setup and cannot adapt or generalize to diverse scenarios. Nor do they deal with multipath fading. They rely on multiple layers of thick and rigid dielectric substrate to host the metasurface, with a fixed placement with respect to the medium interface, both restricting practical deployment. Lastly, these efforts primarily focus on theoretical analysis, lacking end-to-end system design and experimental validation.

Non-RF signals. Other than RF signals, magnetic, acoustic, and light waves have also been explored, which involve various trade-offs in terms of range, datarate, power, hardware complexity, and availability of off-the-shelf hardware. For example, magnetic inductive coupling and, more recently, magnetoelectric effect [2] boast of high power efficiency and small size, but supporting a shorter (2 cm) in-vivo link range than radiative approaches and requiring actively powered coils on the skin. Tarf [8] and AmphiLight [9] use acoustic and laser respectively for air-water links, but adopt application-specific approaches and require specialized endpoints.

Transflective surfaces. Transflective surfaces alter both reflection and transmission through the surface with the same hardware. Intelligent omni-surfaces [54], [55] propose to serve users on both sides, but are limited to theoretical analysis and hardware verification in the anechoic chamber. Existing end-to-end systems [31], [32], [37] switch between transmissive or reflective mode, while we support both modes concurrently to enhance multiple links near the medium interface.

C. Our Approach

We present RF-Mediator, a flexible single-layer metasurface with programmable medium impedance matching and beamforming capability. By matching the impedance of adjacent media dynamically, we *address the root cause of unfavorable signal propagation bahavior* and mask the fact that signals traverse a physical medium boundary, allowing for air gaps and variable-thickness layers. We do not directly tackle signal attenuation or refraction, but account for these via the perceived channel conditions at the receiver and mitigate their effects with beamforming. Moreover, our single-layer design on a flexible substrate improves applicability in diverse scenarios.

Our approach is complementary and orthogonal to existing efforts improving *endpoints*, thus not directly comparable. RF-Mediator can work together with both purpose-built cross-medium endpoints and commodity IoT devices. Further, metasurfaces are low-power passive devices, enhancing through-surface power from external signal sources. Our lightweight design requires no direct contact between the metasurface and the medium interface, decoupling the relative placement of the two via surface programmability.

We focus on RF signals for their relatively long ranges, high datarates, hardware availability and significant interest in them [14], [56]. Conceptually, a metasurface can be added to the medium interface regardless of what signal, e.g., acoustic waves [57], [58], [59], but the specific surface design and the quantitative cost-benefit tradeoffs depend on the signal type.

This paper extends our prior work [1] in three aspects. First, with a new transflective operation mode (Figure 2), we extend from enhancing a single cross-medium link at a time to simultaneously enhancing multiple links on two sides of the interface (Figure 3); Section III-E describes the additional algorithmic steps. Second, we present extensive evaluation results for multi-link support (Figures 18 to 21) and surface flexibility (Figure 28). Third, we present detailed analytical modeling with Equations (2) to (8) and add a discussion section (Section VI).

III. RF-Mediator Design

We first outline the metasurface operational principle, along with a circuit model analysis to identify design requirements. We then describe the hardware design and an efficient multi-stage algorithm for surface configuration.

A. Operational Principle

Metasurfaces alter wave propagation via surface currents induced by incident waves, enforcing a specific electromagnetic boundary condition to allow different fields on both sides of the surface, as per Maxwell's equations [50], [60]. However, medium impedance matching does not happen solely on the metasurface but proceeds via intricate multi-order resonance between the metasurface and the medium/media. We examine wave propagation through a metasurface and an air-tissue interface (Figure 4(a)), to identify the knob for programmability and model diverse deployment scenarios.

Modeling signal propagation. Figure 4(b) shows the analytical model for RF signals traversing the metasurface and an air-tissue interface, where the tissue is a layered composition of skin, fat, and muscle. From the sender on the left, the signals propagate towards and through the surface, any potential gap, then the successive tissue layers. The gap between the surface and tissue, not fixed in thickness, may contain air,

fabric, or other materials, embodying different deployment scenarios. This approach decouples the surface placement from the medium interface location to facilitate deployment. Upon reaching the tissue, the signals navigate through the body's layered composition towards the in-vivo receiver. The total electric field within each medium comprises the forward propagating waves, E^+, and the backward propagating E^- [45]. We want to minimize the reflection, E_0^-, from the interface and maximize the through-interface transmission, E_4^+.

Characterization as circuit components. We extend the basic medium boundary characterization (Section II-A) to analyze the complex interplay between multi-layer medium composition and the metasurface. Waves resonate, i.e., bounce back and forth, between different layers and the surface and also experience various phase delays with respect to the medium segment thicknesses. We model such interactions explicitly, including effects of the surface-medium gap and complex medium composition, with a microwave circuit model shown in Figure 4. Each medium segment is viewed as a transmission line, characterized by its intrinsic impedance *Z*, phase constant β, and length *l*. As the metasurface operates via surface currents, we model the surface as a shunt circuit component with ***surface admittance*** $Y_s = G + jB$ [42], [43], [61]. The *admittance* describes how easily a circuit allows currents to flow, which comprises the *conductance G* (the real part) and the *susceptance B* (the imaginary part). We use admittance (the reciprocal of impedance) here to avoid handling an infinitely large impedance value. The surface element design determines the precise value of surface admittance. Ideally, a lossless surface would have zero conductance, relying on the susceptance *B* for operation. As the admittance increases, stronger surface currents are induced, causing more significant alterations on the amplitude and phase of propagating signals.

Cascading all components. We analyze the circuit components above as a cascade of two-port microwave circuit networks (Figure 4, ports marked with circles). A 2×2 transmission matrix, i.e., the ABCD matrix, can characterize each circuit component. This matrix is defined by the relation between the total electric and magnetic field magnitudes at the two ports. Multiplying successive matrices can then easily capture the multi-order reflections and transmissions between the surface and multiple tissue layers.

For the whole cascaded circuit model in Figure 4, the ABCD matrix is written as

$$\begin{bmatrix} E_0^+ + E_0^- \\ H_0^+ + H_0^- \end{bmatrix} = \begin{bmatrix} A & B \\ C & D \end{bmatrix} \begin{bmatrix} E_4^+ + E_4^- \\ H_4^+ + H_4^- \end{bmatrix} \tag{2}$$

We find the overall ABCD matrix by multiplying known matrices of the surface and tissue layers, which are a shunt circuit component and transmission lines [45].

$$\begin{bmatrix} A & B \\ C & D \end{bmatrix} = \begin{bmatrix} 1 & 0 \\ Y_s & 1 \end{bmatrix} \prod_{k=1}^{3} \begin{bmatrix} \cos\beta_k l_k & jZ_k \sin\beta_k l_k \\ j\sin\beta_k l_k / Z_k & \cos\beta_k l_k \end{bmatrix} \tag{3}$$

where β_k is the phase constant, l_k is the length, and Z_k is the characteristic impedance of the *k*-th medium. Next, we would like to derive the transmission coefficient T (S_{21}) and reflection coefficient Γ (S_{11}) based on the ABCD matrix, since they are the metrics we want to control. They are defined as

$$T = \left.\frac{E_4^+}{E_0^+}\right|_{E_4^-=0}, \quad \Gamma = \left.\frac{E_0^-}{E_0^+}\right|_{E_4^-=0} \tag{4}$$

The electronic and magnetic fields also have the following relation based on plane wave solution

$$\begin{aligned} H_0^+ + H_0^- &= (E_0^+ - E_0^-)/Z_0, \\ H_4^+ + H_4^- &= (E_4^+ - E_4^-)/Z_4 \end{aligned} \tag{5}$$

We assume the last medium, i.e., muscle, is thick enough so that all energy dissipates in this medium. This is true for most scenarios given the high propagation loss of tissue and water. If otherwise, the circuit model can be revised to consider the finite thickness of the medium and add another layer of medium to this model. Here, we assume no significant reflection from other medium will be observed, i.e., $E_4^- = 0$. Then, we substitute Equation 5 into Equation 2. We have

$$\begin{bmatrix} E_0^+ + E_0^- \\ (E_0^+ - E_0^-)/Z_0 \end{bmatrix} = \begin{bmatrix} A & B \\ C & D \end{bmatrix} \begin{bmatrix} E_4^+ \\ E_4^+/Z_4 \end{bmatrix} \tag{6}$$

Then divide E_0^+ for both sides of the equation and substitute Equation 4.

$$\begin{bmatrix} 1 + \Gamma \\ (1 - \Gamma)/Z_0 \end{bmatrix} = \begin{bmatrix} A & B \\ C & D \end{bmatrix} \begin{bmatrix} T \\ T/Z_4 \end{bmatrix} \tag{7}$$

Solving the equation above gives transmission and reflection coefficients based on ABCD matrix values.

$$\begin{aligned} T &= \frac{2}{A + B/Z_4 + CZ_0 + DZ_0/Z_4} \\ \Gamma &= \frac{A + B/Z_4 - CZ_0 - DZ_0/Z_4}{A + B/Z_4 + CZ_0 + DZ_0/Z_4} \end{aligned} \tag{8}$$

The analysis here is different from standard ABCD matrix conversion as we consider wave propagation from one medium (Z_0) to another (Z_4). Compared to Equation 1, the propagation behavior at the interface is no longer solely decided by the medium impedance.

Other medium interfaces. Tissue is the most complex medium due to its layered structure of multiple substances, with non-uniform consistency. The above analysis can be applied to other medium combinations easily, e.g., air-water and air-ground interfaces, which involve matching only two media and are simpler cases than air-tissue interfaces.

Summary. The metasurface alters propagating signals and interacts with the media via its *surface admittance*, as in Equation 3. Therefore, it can change the transmission and reflection coefficients of the medium interface in Equation 8. This offers the knob to match the impedance of different media. However, there are numerous deployment specific factors such as surface-interface gap, medium composition and layer consistency, which motivate dynamic surface configuration.

B. Design Challenges and Requirements

Lightweight design for practicality. The optimal solution for medium impedance matching can be derived analytically with three layers of non-programmable metasurfaces [43].

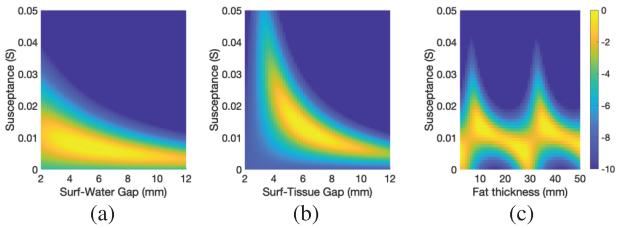

Fig. 5. Heatmaps of through-interface power vs. surface admittance and environmental variation. The desired surface admittance varies with **(a)** **(b)** the surface-interface gap size or **(c)** the fat layer thickness. This highlights the necessity of surface programmability.

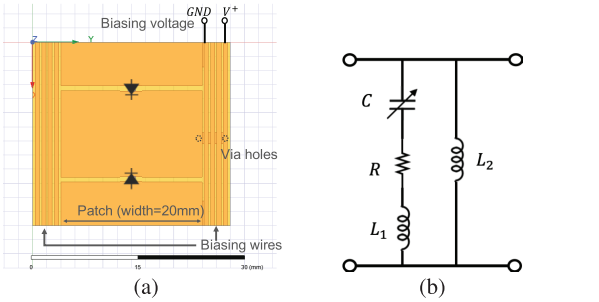

Fig. 6. Metasurface Design. **(a)** Surface element. **(b)** Equivalent LC circuit. We control the voltage applied to varactor diodes with individual biasing wire for each element.

However, a 3-layer surface, fitted at the medium interface, is cumbersome for deployment due to the multi-layer substrate thicknesses. Instead, we aim for a single-layer design, which offers simplicity, low hardware cost, and minimal thickness for mechanical flexibility. Our simulation results suggest a single layer is already able to achieve near-optimal impedance matching (less than 1 dB loss). Further, instead of requiring a fixed gap or direct contact, we decouple the surface placement from the interface position, allowing a varying surface-interface gap.

Appropriate admittance for matching. We use the circuit model to numerically model signal propagation in diverse deployment scenarios to find appropriate surface admittance values. For any given surface admittance Y_s, we can calculate the ABCD matrix (Equation 3), and then the transmission and reflection coefficients (Equation 8). Figure 5 shows the power transmitted through the medium interface when using different surface admittance values in scenarios with various surface-medium gap sizes or fat thicknesses. The higher the through-interface power, the lower the reflection, and thus, the better the medium matching performance. We can achieve near-optimal through-interface transmission (only 0.5 dB loss) by using an appropriate surface admittance ranging from 0 to over $0.05j$. However, such a large surface admittance range is challenging since drastically different surface patterns are often needed to cater to less than $0.01j$ change [42].

Dynamic adaptation for robustness. Based on the previous analysis, there is no one-size-fits-all surface admittance value. Several factors affect the appropriate surface admittance (Figure 5): (i) The gap between the surface and medium interface, hardly controllable in practice. The smaller the gap, the larger the admittance to maintain a high through-interface transmission power. (ii) Different medium pairs, medium composition and consistency. An air-tissue interface needs a much higher admittance than an air-water interface. Moreover, the fat thicknesses vary significantly from one person to another and even between different body parts of the same person, which affect the needed admittance significantly. (iii) The previous circuit model analysis and simulations used an approximate tissue model and lab-measured medium parameters, both simplified from real scenarios. The remaining systematic errors could degrade the surface performance by 2-3 dB, and we can use surface programmability to account for that.

Thus, we aim to design a single-layer programmable metasurface covering the desired surface admittance tuning range, from $0j$ to over $0.05j$. This provides sufficient programmability to adapt to the above dynamics, as shown in Section V-E.

Operational frequencies. We focus on 2.4 GHz, but the design can be adapted to other frequencies like 900 MHz or 5 GHz by scaling the metallic pattern geometry. Several proposals [7], [62], [63] exploit 2.4 GHz Wi-Fi radios as ambient signal sources to provide backscatter connectivity. This could significantly lower the hardware requirement and make in-vivo networking more accessible. Moreover, antenna size is inversely proportional to frequency and the small antenna size of 2.4 GHz is crucial for in-vivo devices [14].

C. Hardware Design

Surface elements. Our surface design consists of an array of basic repeating units as *elements*, each with two rectangular patches connected by varactor diodes (Figure 6(a)). This simple yet effective surface pattern is inspired by designs for other purposes [31], [64], [65]. The metallic patches act like antennas, resonating with incident signals and inducing surface currents. The varactor diodes work as tunable capacitors, controlled by biasing voltages, to alter the electronic responses and produce the desired surface admittance. All surface elements share a common ground wire as the voltage reference, while each element has a separate biasing wire, connected through via holes. This permits element-wise surface admittance control for both medium impedance matching and beamforming.

Achieving programmability. The equivalent circuit for the surface element is shown in Figure 6(b), where C is the tunable capacitance of the varactor, R is the resistance of the varactor, L_1 is the inductance of each patch, and L_2 is the inductance of biasing wires. The surface admittance is

$$\begin{aligned} Y_s &= \frac{1}{\frac{1}{j\omega C} + R + j\omega L_1} + \frac{1}{j\omega L_2} \\ &= \frac{\omega^2 C^2 R + j\omega C(1-\omega^2 CR)}{(1-\omega^2 CL_1)^2 + (\omega CR)^2} - \frac{j}{\omega L_2} \\ &\approx \frac{\omega^2 C^2 R}{(1-\omega^2 CL_1)^2} + \left(\frac{\omega C}{1-\omega^2 CL_1} - \frac{1}{\omega L_2}\right) j \end{aligned} \quad (9)$$

For our design, we have $(\omega CR)^2 \ll (1-\omega^2 CL_1)$, thus allowing for the approximation in the last step. We observe that the tunable capacitance C is the dominant factor for the susceptance (the imaginary part of admittance), which enables programmability. The conductance (the real part of admittance) is proportional to the resistance R, which causes additional power loss on the surface. To minimize the loss and maximize tunability, we need to use varactors with a small resistance but a large capacitance tuning range.

TABLE II
VARACTOR PERFORMANCE VS REVERSE BIAS VOLTAGE

Voltage (V)	30	20	15	10	5	0
Capacitance (pF)	0.71	0.81	0.90	1.0	1.32	3.72
Resistance (Ω)	0.26	0.3	0.36	0.38	0.45	0.63

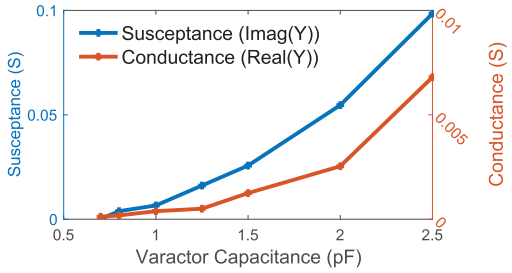

Fig. 7. Surface admittance versus capacitance. Increasing the varactor capacitance also increases the surface admittance; The real (lossy) part of admittance is kept low.

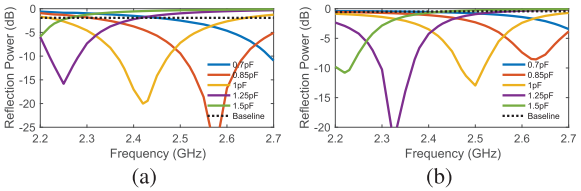

Fig. 8. Reflection reduction over frequency. With appropriate varactor capacitances, the surface reduces the reflection by over 10 dB for **(a)** water and **(b)** tissue at around 2.4 GHz.

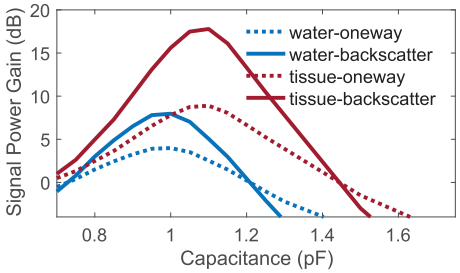

Fig. 9. Cross-medium transmissive power gain.

Achieving desired admittance range. Our surface design needs to expose the desired tunable admittance range mentioned above; Otherwise, impedance matching cannot be achieved whatever the surface tuning algorithm. The admittance range depends on the geometry of the metallic pattern, the specific choice and placement of varactors, the wiring for applying biasing voltage. The limited capacitance tuning range of varactors is also a hard constraint.

Specifically, we choose SMV1405 [66] varactor diodes and run SPICE [67] simulations to derive the capacitance and resistance verses bias voltage (Table II). Given the varactor and its capacitance range, we derive a specific surface metallic pattern to achieve the desired admittance, guided by Equation 9. To increase the ratio of susceptance and varactor capacitance, we can lengthen the surface patch for higher L_1; To decrease the susceptance by a constant, we can increase the width of the biasing wire for lower L_2. Through iterative HFSS [68] simulations, we arrive at the final pattern shown in Figure 6(a). The pattern geometry is precisely tuned, e.g., a pattern 2 mm smaller in width and length has only half of the tunable admittance range and shifts the range partly to negative admittance values. Previous varactor-based metasurfaces lack considerations for our problem and cannot be used; They may have a small tunable surface admittance range anywhere in the entire design space, $-\infty j$ to ∞j, far off the desired range.

This way, our programmable metasurface can suit various situations, obviating environment-specific, non-programmable surfaces. Figure 7 shows the surface admittance under different varactor capacitance values. The susceptance varies from $0j$ to over $0.05j$, while the conductance remains one order of magnitude lower than the susceptance. This shows we indeed achieve a large admittance tuning range while maintaining a low power loss on the surface. We primarily use the 0-2 pF capacitance range, to avoid higher resistance power loss and non-uniform admittance values over the 2.4 GHz frequency range, both degrading matching performance.

Impedance matching simulation. To verify the medium impedance matching performance, we run HFSS [68] simulations for surfaces placed near air-tissue and air-water interfaces. First, we examine the reflection power changes as shown in Figure 8. With an appropriate capacitance of varactors (around 1 pF), the surface can achieve over 10 dB of reflection reduction, corresponding to about 50 MHz of operational bandwidth for both water and tissue. The reflection trough shifts to neighboring frequencies when the capacitance of varactors is slightly different. The power transmitted through the interface exhibits a reversed trend over frequency, i.e., higher transmissive power with an appropriate capacitance. We show the transmission power gain versus capacitance in Figure 9, with a max gain of 4 dB and 9 dB for air-water and air-tissue links, respectively. Almost all incident power is transmitted through, but the air-tissue interface has a worse baseline, resulting in a higher gain.

Our surface provides equal gains for both propagation directions. Assuming the scattered signal strength is proportional to the strength of signals reaching a backscatter device [3], the backscatter power gain equals the sum of (dB-scale) gain values in two directions. We achieve gains of up to 8 dB and 18 dB for backscatter devices in water and tissue respectively. Next, we simulate the effect of endpoint depth (distance from the medium interface to the endpoint) and medium conductivity in Figure 10. We run other simulations with no conductivity to isolate the performance of medium impedance matching, but the experimental evaluation section naturally includes the influence of conductivity. For both air-water and air-tissue, the transmissive power gain remains constant regardless of the in-vivo endpoint depth. If we consider medium conductivity, the received power decreases when depth grows, while our surface provides a high gain regardless.

We further simulate the programmability provided by the varactors with a varying surface-interface gap and a varying fat layer thickness. Our surface design maintains a high power transmitted through the interface by choosing suitable capacitance values, agreeing with Figure 5.

Surface size. Previous simulations assume an infinite surface, while a finite surface may have different properties. We verify with simulations that a surface with 4×4 elements suffices. Once above this minimum element count, the size

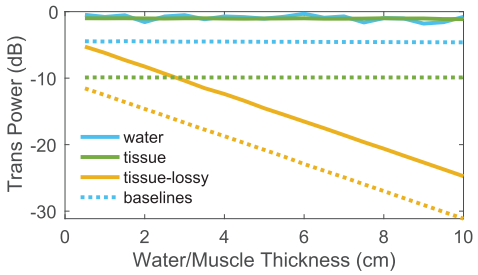

Fig. 10. Power gain at various in-vivo depths.

of the surface should match the application scenarios. A larger surface provides a larger coverage area and higher beamforming gain.

Beamforming. Endpoints in challenging media, such as water or tissue, often experience destructive multipath fading [5]. Since medium impedance matching only boosts the transmission through the metasurface and medium interface, further signal propagation can still be susceptible to multipath effects (Figure 14). Fortunately, we can apply a distinct biasing voltage to control per-element matching behavior, which provides element-wise on-off amplitude control on through-surface signals, without additional onboard RF switches. This is a separate functionality leveraging the element-wise impedance-matching capability to mitigate multipath fading, achieving beamforming gain on top of medium matching gain. Our single-layer design does not have the full range of phase control for beamforming, although it is achievable with more layers stacked. Previous work already discussed the performance margin [32], so we choose a one-layer design for its simplicity and deployability.

Surface shape and coupling. Surface shape perturbations affect the beamforming performance, but not the impedance matching functionality; The surface admittance range, primarily influenced by the metallic pattern dimensions, is not sensitive to the substrate shape. This resilience is akin to flexible antenna designs, where shape perturbations minimally affect the resonance frequency, agreeing with metamorphic surfaces [36]. Simulations across several shapes confirm negligible impedance matching discrepancies against planar counterparts (Section V-G). A more drastic shape deformation like folding or rolling the surface [38], does not match our intended application scenario. Nonetheless, unexpected coupling between the surface and the non-air medium can occur when they are placed in proximity. Fortunately, our programmability allows for adjustments to counteract coupling effects.

D. Control Algorithm

We present an efficient multi-stage algorithm to determine element configurations, i.e., the element-wise voltage values, to optimize received signal strength of wireless links with joint medium impedance matching and beamforming. First, it explicitly performs coarse-grained medium impedance matching to reduce the search space; Second, it performs beamforming based on the medium matching results; and lastly, it performs fine-grained voltage tuning to account for any inaccuracy. Eventually, a portion of the surface elements *transmit* signals with impedance matching, while the rest *reflect* signals that would produce destructive multipath fading. We first describe the algorithm for a single, through-interface link and extend it to enhance multiple links concurrently in the next subsection.

Channel model. We consider the multipath channel between the TX (transmitter) and the RX (receiver)

$$h_{T-R} = \sum_{i=1}^{i=N} s(V_i)\ h_i + h_{env} \tag{10}$$

where h_{env} is the collective channel coefficient representing all signal paths not going through the surface, N is the number of surface elements, $s(V_i)$ is a complex number representing the amplitude and phase changes caused by impedance matching effect of surface element i, V_i is the voltage applied, and h_i is the channel coefficient characterizing all paths going through element i. The goal is to set appropriate surface configurations, i.e., the voltage for each surface element, to maximize the received signal strength $\|h_{T-R}\|$ based on the endpoint feedback of the received signal strength.

Challenges. The optimal surface performance arises from both medium impedance matching and beamforming. However, there is no way to completely tease apart these two effects from the endpoint perspective. Further, the effect of impedance matching, $s(V_i)$, is not a fixed function of the voltage applied, V_i, that can be measured in advance; Many factors affect medium impedance matching as discussed in Section III-B. Finally, a brute-force search enumerating all surface configurations is impractical; Considering our implementation, 8 discrete voltages each for 64 surface elements, the search space (8^{64}) is too large. Further, this is not a convex optimization problem as multiple local and global optima can exist. Given the specific challenges here, existing surface control algorithms, such as what RFocus [32] uses or a closed-box optimization, do not work due to lacking both software and hardware considerations for cross-medium challenges.

Multi-stage solution. We divide and conquer this problem with a multi-stage control algorithm that performs medium impedance matching, beamforming, and refinement successively. In the first stage, we explicitly probe the medium matching performance, $s(V)$, to reduce the search space by applying a uniform voltage V to all surface elements. The channel equation above can be written as

$$h_{T-R} = s(V) \sum_{i=1}^{i=N} h_i + h_{env} \tag{11}$$

With a high probability, $\sum_{i=1}^{i=N} h_i$ is much larger than noise. The changes in $s(V)$ can be observed from the changes in h_{T-R} with different voltages applied. We record the two voltage states, V_1 and V_0, that respectively maximizes and minimizes the endpoint signal strength ($\|h_{T-R}\|$), as the input for the next stage. Note that without knowing how the signal phase is aligned with h_{env}, we can not tell which state is maximizing $\|s(V_i)\|$ or minimizing it. Fortunately, we only need to know that these two states create the opposite effects.

In the second stage, we use the recorded states, V_1 and V_0, as on-off control for beamforming. We perform a majority voting procedure to find the best on-off configuration. Specifically, we want to determine the sets of elements adopting the on and

off states respectively, S_1 and S_0. The channel we want to improve can be re-written as

$$h_{T-R} = s(V_1) \sum_{j \in S_1} h_j + s(V_0) \sum_{i \in S_0} h_i + h_{env} \quad (12)$$

We batch test random on-off configurations of the surface and record the corresponding received signal strength from endpoint feedback. After testing all configurations, we count votes for each surface element. If a configuration leads to a higher signal strength than the median strength of all configurations, we cast a vote for each turned-on element in this configuration. Otherwise, we cast a vote for each turned-off element. An element is marked as *on* (S_1) if it receives votes from more than half of the tested configurations, or *off* (S_0) otherwise. For our surface prototype with 64 elements, we set the batch test number to 128 random configurations, which is significantly fewer than all 2^{64} possibilities. Setting the number of random configurations to twice the number of elements achieves a good balance between performance and feedback overhead; The extra gain of testing more configurations diminishes empirically. Figure 26 experimentally compares this algorithm with enumerating all configurations.

In the third stage, we refine V_1 and V_0 by testing the respective adjacent voltage values without changing the on-off element sets, S_1 and S_0. We update V_1 and V_0 for the respective element sets if a higher received signal strength is achieved. This aligns the phase of h_{env} with that of through-interface signals and accounts for any inaccuracy in stage one.

Control granularity. We use 8 voltage values (30, 20, 15, 10, 5, 2.5, 0) in the control algorithm. These values are chosen empirically to cover the tunable surface admittance range. Using more voltage values can bring additional performance gain, but requires more feedback measurements. Another design choice about control granularity is that we utilize element-wise control of the surface. Figure 26 shows the extra gain from element-wise control over column-wise control.

Feedback mechanism. We use the received signal strength (RSS) as the feedback metric to guide our algorithm, which is accessible across diverse wireless hardware and standards. As shown in evaluation section, we can acquire RSSI (received signal strength indicator) directly from commercial ESP32 Wi-Fi devices. Due to the reciprocity of metasurface operations, feedback from either end of the cross-surface link is sufficient; We collect feedback from in-air (AP) devices only, avoiding overhead for in-body or in-water devices. We can potentially avoid feedback by incorporating sensing hardware as in LAVA [35]. For backscatter devices, we use the received backscatter signal strength measurement from the in-air endpoint, similar to In-N-out [3]. There is usually a margin between sufficient RSS for useful links and minimum detectable RSS for feedback. When endpoints are undetectable initially, we can potentially perform blind impedance matching and beamforming, using sub-optimal configurations to power up (backscatter) devices.

E. Supporting Multiple Links

The algorithm above aims to enhance single links that cross the medium interface. However, often multiple endpoint devices near the surface, on both sides of the medium interface, need connectivity enhancement. For example, multiple in-body devices for medical monitoring and actuation, together with on-body (in-air) wearable wireless devices, can suffer from unreliable connectivity with the AP as shown in Figure 3. These devices can transmit interleaved packets, but switching surface configurations for each link would require cumbersome and costly high-speed digital circuitry for rapid packet-level reconfigurations. Alternatively, using MU-MIMO or OFDMA techniques, these devices can transmit or receive packets simultaneously. Without modifying or assuming the MAC layer design of wireless endpoints, our goal is to provide concurrent link enhancement for multiple endpoints, regardless of their position relative to the medium interface.

We opt for a joint enhancement strategy, leveraging two opportunities: (1) multiple in-body devices can share the medium matching benefit, and (2) on-body wearable devices in the air can utilize the reflection from the turned-off surface elements for enhancement, by altering channel conditions and beamforming. Due to the transflective nature of our surface, its operation influences both transmission and reflection simultaneously. With a proper control algorithm, a single surface configuration can simultaneously boost signal strengths of multiple links as a shared infrastructure.

Specifically, we follow the same procedure for the single-link control algorithm but adjust the optimization objective function at each stage as follows: (i) During the first medium matching stage, we use the link strength between in-air AP and the in-body device(s) as feedback to probe the medium impedance matching performance. If the in-body device(s) is inactive or absent, we use the signal strength of the (in-air) *on*-body device link(s). (ii) For the next two stages, we use the sum of dB-scale received signal power from all links as

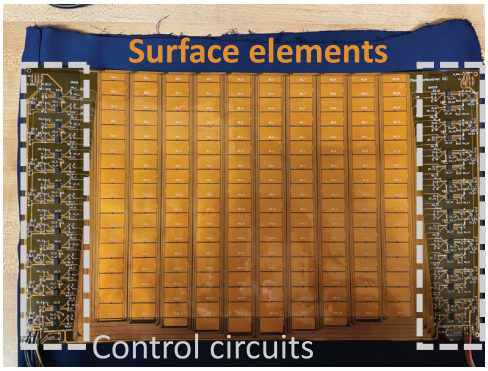

(a) Surface prototype as a flexible PCB. The control circuit is currently placed on the sides to ease soldering. Further circuit integration can enable a smaller form factor.

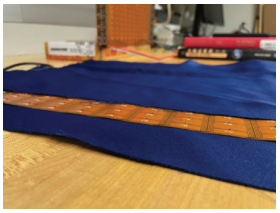

(b) 0.1 mm in thickness.

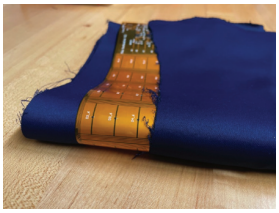

(c) As flexible as fabric.

Fig. 11. Surface hardware implementation.

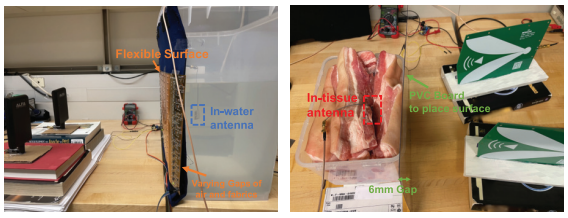

(a) (b)

Fig. 12. Experiment setups. **(a)** Air-Water interface. **(b)** Air-Tissue (pork belly) interface. We use fabric layers or a plastic board to host the surface; fabric and plastic exhibit similar permittivity to air compared to water or tissue.

the feedback metric and objective of the joint optimization process. This approach benefits links that need significant improvement, such as those experiencing poor channel conditions. We can also use other joint optimization strategies according to the specific application scenario.

IV. Implementation

Surface fabrication. We fabricate the surface using commercial flexible PCB fabrication process and manually solder circuit components including the SMV1405 varactors [66] (Figure 11(a)). A surface prototype is as thin as a piece of paper, about 0.1 mm thick (Figure 11(b)), and as flexible as fabric (Figure 11(c)). This facilitates flexible surface deployment, e.g., as a metasurface blanket or T-shirt for medical monitoring. Additional plastic lamination can waterproof the surface for diverse scenarios. Due to limitations of the fabrication process, the area size of our surface prototypes is capped at 24×40 cm, with 8×10 elements. We individually control the voltages of 64 elements, while the remaining 16 act as padding to avoid surface edge effects. Fabricating each piece of surface costs 50 and the circuit components cost around 100, 1.5 per tunable element. The cost can be much lower for large scale production due to economies of scale.

Control circuit. Since varactors hardly draw any current, we design a lightweight varactor voltage control circuit. For a small form factor, we integrate the control circuit on the surface to avoid external DAC devices. We use 16 4-channel DAC MPC4728 chips [69], each connected to two LM358 OP amplifiers [70] to amplify the voltage from 0–4 V to 0–36 V. We prioritize the ease of soldering for the current layout, while a highly integrated PCB implementation can achieve a smaller form factor. A PC with Intel I7-7700 acts as the controller, collecting feedback and computing surface configurations with Matlab; These are then sent to an ESP32 [71] over Wi-Fi to configure the DAC chips through two I2C buses.

Control latency. To adapt to environmental dynamics, such as endpoint or user movement and surface shape changes, we need to run the control algorithm for surface reconfiguration. Our current implementation does not explicitly optimize for a minimal latency. The latency for such adaptation comprises three parts: (i) collecting feedback from in-air endpoints, (ii) computing desirable surface states, and (iii) setting surface hardware states. For surface systems, the last part, i.e., updating voltages, typically dominates the adaptation latency. Each I2C bus provides a bandwidth of 3.4 Mbps [69] in the high speed mode. It takes 9 bytes to transfer the voltage data to one chip, so only 0.17 ms to set 16 chips using 2 buses. Our control algorithm goes through 3 exploration stages, which requires 8, 128, and 9 instances of setting surface states respectively. The latency of feedback collection is dominated by the time taken to send feedback from the in-air endpoint to the surface controller. We only need one aggregated feedback transmission for each algorithm stage, making the delay negligible. Hence, we can explore the search space in less than 25 ms with fully optimized microcontroller code, which is fast enough for most dynamic scenarios.

Power consumption. Our surface element design is passive and consumes little power. The varactors are reverse-biased and draw a maximum of 20 nA of reversed current [66], or less than 1.2 uW power per surface element under a 30 V bias voltage. The power consumption of all surface elements in our implementation is less than 100 uW, close to the power footprint of many backscatter designs [62], [63], within the capability of ambient signal power harvesting. Our current control circuit is designed for precise voltage control to validate and characterize the surface performance, not optimized for low power consumption. The total power consumption of 16 DAC chips [69] and 64 OP amplifiers [70] is around 500 mW. Optimizing control circuit power consumption is not the focus of this paper as it is largely an engineering task. A more specialized control circuit can reduce power consumption significantly. For example, using analog voltage dividers and multiplexer chips [72], we can control surface elements with a few discrete voltages, reducing the quiescent power consumption of the control circuit to around 100 uW.

V. Evaluation

We start with validating the medium impedance matching capability and then end-to-end performance gain. To highlight the benefits of programmability, we compare with a non-programmable surface when subjected to environmental dynamics. We also perform microbenchmarks of system operations and effectiveness. Lastly, we highlight the necessity and performance of a bent flexible surface using simulations.

A. Experiment Setup

Media studied. We mainly study the performance of RF-Mediator for air-water and air-tissue (emulated with pork belly) links. The property of ground (soil) is dictated by the water it contains [73], so we expect the performance for air-to-ground links to be similar to air-to-water links. We place water and pork belly in plastic containers (Figure 12) and place the surface in front of the test medium with a default air gap of 5 mm. Although there are fabric layers and a plastic container between the surface and the other test medium, they exhibit similar permittivity to air, in contrast to water and tissue [74], [75]. Moreover, fabric layers are not solid material and most of their volume is taken up by air. Thus, they can be treated as air in terms of the medium-specific signal propagation behavior.

We conduct most experiments with a water container (Figure 12(a)), as it is much easier to experiment with and sample endpoint locations inside water than tissue. The container is similar to human upper body in size, so we can emulate air-to-tissue links for medical devices. Impedance matching for

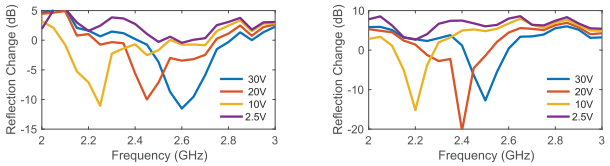

(a) Water (b) Tissue

Fig. 13. Reflection reduction over frequency. Matching medium impedance reduces reflection by over 10 dB. The biasing voltage should be set to match the center frequency of the links (the red line, trough showing minimal reflection).

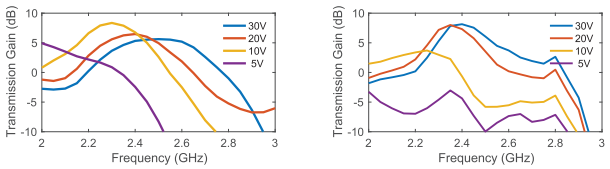

(a) Water (b) Tissue

Fig. 14. Transmissive power gain over frequency. With an appropriate voltage, impedance matching increases through-interface power by over 5 dB, although multipath reflections inside the water/tissue containers affect results.

air-water and air-tissue interfaces follows the same principle, as described in Section III-A, and both water and tissue experience similarly difficult channel conditions [6]. Nevertheless, to further verify the system, we show the performance gain for air-tissue links in Figure 15 and Figure 25.

Link setup. We set up 2.4 GHz links for experiments using USRP N210s [76] unless otherwise noted. We use directional patch antennas [77] for in-air endpoints and (water-proof) omni-directional flexible antennas [78] for in-water and in-tissue endpoints (connected to USRPs with coaxial cables). To sample various channel conditions, we move both endpoints, creating different incident angles for the incoming signal to the medium interface, at up to 45 degrees. We use the received signal strength (RSS) of the in-air endpoint as feedback for all experiments, as it is easier to obtain than in-water or in-tissue endpoints. Due to channel reciprocity, the channel feedback in both directions only differs by a constant in our experiments, so both can guide the control algorithm and yield similar results. We also set up 2.4 GHz Wi-Fi links with a bandwidth of 20 MHz using ESP32 endpoints [71] to measure throughput and show wideband operation capability. For all experiments, we remove the surface to measure a faithful baseline power.

Surface shapes. Controlling flexible surface shape perturbations precisely and repeatably is very difficult. However, during experiment, random shape perturbations arise as surfaces are removed (and redeployed) for baseline measurements across different links. We model such perturbation implicitly as channel variation and rely on surface programmability to address it. Moreover, our surface naturally took on a curved shape as shown in Figure 12(a). This curvature results from the container's deformation under the weight of the water, up to 40 qt and weighing over 70 lb when full. Such macroscopic shape perturbation, akin to a blanket covering the stomach of a lying individual, represents typical deployment scenarios.

B. Medium Impedance Matching Validation

We first verify the fundamental hardware functionality, i.e., medium impedance matching. To avoid conflating with the control algorithm performance, we manually apply selected voltage to all surface elements uniformly here to focus on the matching performance without the additional beamforming gain. We place RF absorbing foam [79] around the setup to minimize multipath effects (for this experiment only).

Reflection reduction. We first measure the reduction of reflection power from the medium interfaces. We set up a short link using two directional Vivaldi antennas, around 30 cm apart, both pointing towards the surface and the water/tissue containers at a small angle (Figure 12(b)). This distance roughly ensures we only measure the most direct reflection path from the surface and medium interface. We measure the reflection power strength when the surface is deployed and subjected to different bias voltages. Figure 13 shows the surface reduces the reflection by over 10 dB around 2.4 GHz, compared to the surface-free baseline, for both air-water and air-tissue interfaces. This shows that appropriate voltages can result in good medium impedance matching, i.e., large reflection reduction, agreeing with the results in Figure 8. The shift of matching troughs with decreasing voltage also agrees with Figure 8, which indicates an increased surface admittance as expected when the voltage decreases. The exact voltage needed (20 V) for medium impedance matching on 2.4 GHz is different from the simulated value (10 V). This is because simulations rarely capture practical deployments perfectly, due to real-world constraints like surface-medium gaps and varying tissue layer composition and consistency.

Through-interface transmission boost. The reduction in reflection should correspond to an increase of through-interface signal power. Figure 14 verifies this through the received signal power gain on the in-water and in-tissue antennas. Without running our control algorithm, we see over 5 dB in power gain when an appropriate voltage is selected, which matches Figure 9. The reflection power from the medium interface is stronger and easier to measure, while the in-water or in-vivo received signal power is susceptible to multipath fading inside the container, leading to irregular curves; Thus, we expect only a qualitative match-up. This highlights the necessity of dynamic surface adaptation to counter multipath effects and other environmental changes.

C. Boosting Cross-Medium Links

Next, we activate the control algorithm to assess the end-to-end link improvement from RF-Mediator, with gains from both medium impedance matching and beamforming.

Received signal strength gain. We experiment with 45 air-water and 30 air-tissue links. Specifically, we place the in-water antenna at 3 locations (5, 7.5, 10 cm away from the air-water interface inside the water container), 5 different locations each, while the in-air endpoint is placed at 3 locations (25, 35, 50 cm away from the metasurface). This is the default setup unless otherwise noted. RF-Mediator boosts the received signal power of in-water endpoints by a median of 7.2 dB and up to 22 dB (Figure 15). For air-to-tissue links, we experiment with 2 in-vivo endpoint locations and 15 in-air endpoint locations. The results show a median gain of 8.2 dB and up to 17.5 dB for the in-vivo received signal power. Thus, our system can effectively match the impedance between air and tissue despite the challenging multi-layer structure of tissue.

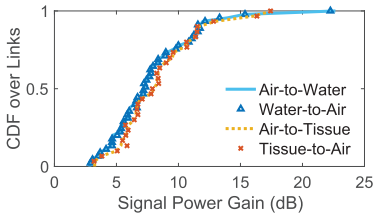

Fig. 15. Received signal power gain for bi-directional cross-medium links.

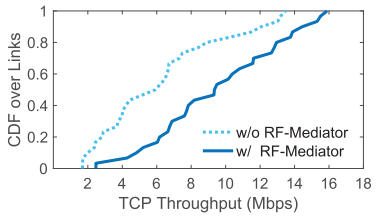

Fig. 16. TCP throughput improvement for air-water Wi-Fi links.

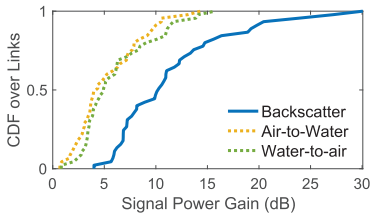

Fig. 17. Gain for emulated backscatter links.

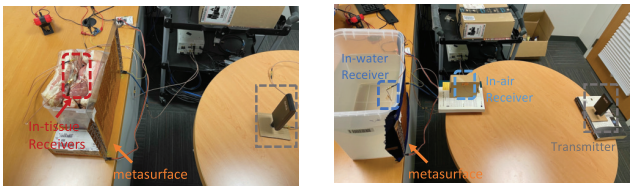

(a) Two in-tissue links (b) In-water and in-air links

Fig. 18. Multi-link experiment setups.

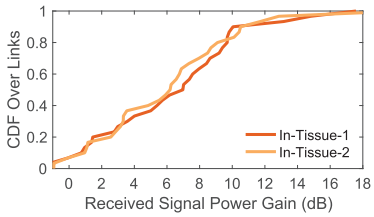

Fig. 19. Received signal power gain when concurrently enhancing two in-tissue devices at different locations.

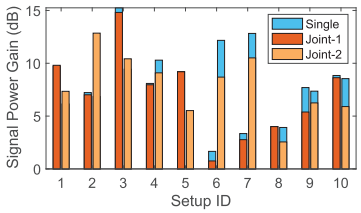

Fig. 20. Performance comparison between enhancing two links jointly and enhancing them separately.

To put the gain in context, the signal-to-noise ratio (SNR) of air-to-tissue links in a state-of-the-art medical prototype [14] is around 10 dB and can be negative due to channel variation. RF-Mediator provides extra link budget, enabling longer and more reliable links or higher throughput.

Bi-directional gain. Figure 15 shows the received signal power gain from water or tissue to air, i.e., the reversed link direction. The gains in both directions match well for individual links, confirming direction-agnostic gains due to channel reciprocity. The gain for tissue-air links is higher than for water-air links. This agrees with the simulation results in Figure 9, but the extra gain is smaller for several possible reasons. We use multiple pieces of pork belly to construct the in-vivo environment, inadvertently leaving some air gaps (air-based propagating paths) in between. This can produce a higher surface-free baseline power, thus lowering the gain from the surface. Another reason is that each piece of pork has a different fat layer thickness, creating challenging discontinuities in the medium composition for impedance matching.

Throughput improvement. To show the throughput increase brought by the signal power gain, we measure TCP throughput with `iperf` for 45 air-to-water Wi-Fi links with and without the surface. The air-water links are set up as mentioned above, except that we use the widely used IoT hardware, ESP32 [71], as the endpoints. The Wi-Fi RSSI from the in-air endpoint is the feedback to the control algorithm. We place a flexible antenna [78] in the water as the in-water endpoint, and connect it to an ESP32 via a cable. The transmit power is set to 0 dBm to emulate devices with a tight power budget, following [14] and [35]. Figure 16 shows our surface achieves a median throughput increase of 55%, and up to about 400%.

Backscatter links. As discussed in Section II-A, we expect up to double the gain seen above for backscatter links since the signals traverse the medium interface twice. We use 2 USRP N210s as the in-air transmitter and receiver, and another USRP connected to a flexible antenna in the water as the backscatter device. Existing backscatter devices often shift the backscatter signal frequency to avoid self-interference [5], [7], [63]. Thus, we shift the backscatter-to-receiver channel (central frequency) by 20 MHz relative to the transmitter-to-backscatter channel. This means our system needs to support two separate channels simultaneously. Since backscatter signals traverse both channels, we multiply the channel coefficients in both directions to emulate the overall channel coefficient of backscatter links. Here, we assume the backscatter power is proportional to the incident power [3], [5]. Our control algorithm takes the amplitude of the overall channel coefficient as feedback to match practical settings. We place the in-air transmitter and in-air receivers at 3 locations and test 15 in-water backscatter locations, measuring 45 links in total. Figure 17 shows RF-Mediator provides a median gain of 10.3 dB and up to 30 dB for the received signal power. The gain comes from both the transmitter-to-backscatter (air-to-water) and backscatter-to-receiver (water-to-air) directions.

Endpoint-surface distance. As the surface can not cover the whole medium interface, only part of the incident signals traverses through the surface. We set up 15 air-to-water links, varying the distance between the surface and the in-air endpoint. Figure 22 shows the performance degrades slowly over distance but still boosts the through-interface power.

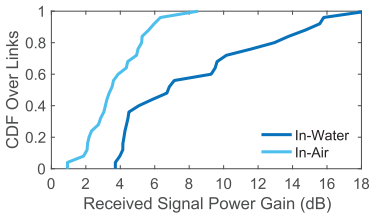

Fig. 21. Received signal power gain when concurrently enhancing one in-water and one in-air devices.

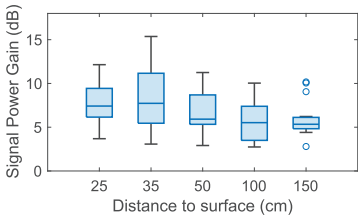

Fig. 22. Surface-endpoint distance.

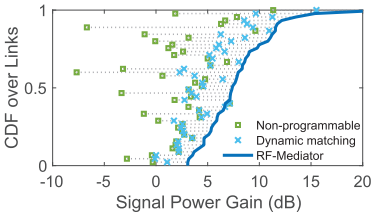

Fig. 23. Need for programmability.

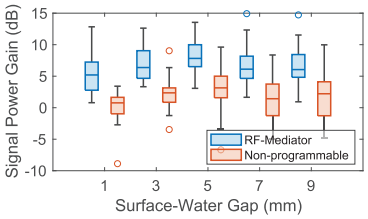

Fig. 24. Surface-interface gap.

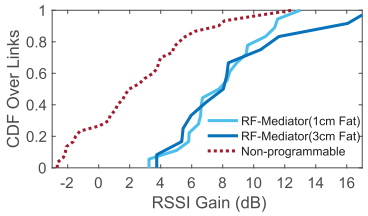

Fig. 25. Adaptation for different fat thicknesses.

D. Supporting Multiple Links

As discussed above, our metasurface can function as the shared infrastructure for multiple wireless links instead of only a single link or endpoint. We set up links between one in-air AP (transmitter) and two in-tissue devices (receivers) in Figure 18(a) and experiment with 30 sets of in-tissue device locations. Figure 19 shows that, with a single shared metasurface configuration, we can achieve a median gain of 6 dB and up to 18 dB receiver signal power gain for two in-tissue receivers concurrently. We further evaluate the performance gap between joint enhancement and individual enhancement. Comparing our algorithm to optimizing the surface configuration individually for each device, we notice only a slight performance dip (Figure 20).

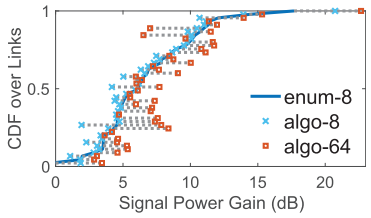

Fig. 26. Algorithm variant comparison.

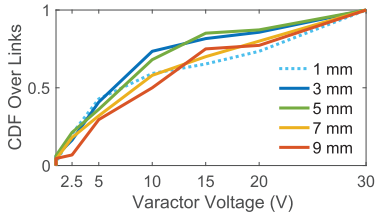

Fig. 27. Selected varactor voltage vs. surface-interface gap.

Our system extends benefits to in-air wireless links near the medium interface. This is advantageous in medical settings, where on-body wearable wireless devices need enhanced reliability. We set up links between one in-air AP (transmitter) and one in-tissue device and one in-air on-body device (receivers) in Figure 18(b) and experiment with 25 sets of in-tissue and on-body device locations. Our metasurface provided a median gain of 3 dB and up to 8 dB for the in-air on-body device (Figure 21), while maintaining a median gain of 7 dB and up to 18 dB for in-tissue device. Although the gain for in-air devices is less compared to in-water due to the absence of impedance matching, it nonetheless contributes to the reliability of in-air wireless devices like on-body wearables.

E. Benefits of Programmability

Programmability gain breakdown. We perform ablation study on RF-Mediator by gradually removing its programmability capability (Figure 23). For reference, RF-Mediator provides a median gain of 7.4 dB for 45 air-water links. If we omit element-wise beamforming control and instead apply uniform voltage to all elements, dynamic medium impedance matching alone provides a median gain of 4.5 dB. This roughly matches the results in Figure 14(a), but is more affected by the specific multipath channels. If we further remove dynamic voltage control and instead use a fixed, predetermined best voltage (15 V) for all links, such a "non-programmable" surface yields only a median gain of 2 dB. The non-programmable surface also incurs up to 7.6 dB of power *loss* due to channel variation, significantly affecting the system usability, while RF-Mediator provides at least 3 dB gain for *all* links by adapting to the channel (i.e., applying dynamic voltage settings). This shows that surface programmability provides a beamforming gain and handles channel fluctuations effectively.

Robustness to surface-interface gaps. We evaluate system performance when adapting to a varying gap, produced by different numbers of fabric layers, between the surface and the water container. Each fabric layer adds around 2 mm and the container wall is around 1 mm thick. We test 0 to 4 fabric layers, i.e., 1 to 9 mm gap, with 30 air-to-water links each. Figure 24 shows a median gain of over 5 dB of

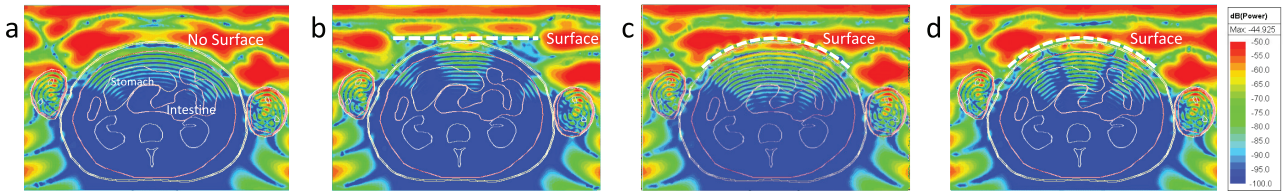

Fig. 28. Simulated power distributions over the human body cross-section: (a) without metasurface, (b) a planar surface (white dashed line), (c) a curved flexible surface with a uniform voltage/capacitance, (d) a curved flexible surface with beamforming.

and up to 15 dB for all gap sizes, which demonstrates the effectiveness of surface adaptation. Theoretically, the largest gap our design can cater to is up to 1.2 cm (Figure 5) without performance degradation; This is sufficient for most scenarios, for example, when the user is covered in a gown or blanket. The best performance is observed for the 5-mm gap, and the worst at 1 mm, which is consistent with Figure 5(a), but a high gain can be achieved regardless of gap size. For a non-programmable surface that applies a (best-matched) uniform voltage to all elements, its median gain is around 5 dB lower than RF-Mediator and the worst-case performance incurs over 10 dB power loss. This again confirms the need to adapt to environmental fluctuations.

Robustness to fat layer thickness. The thickness of the fat layer affects the capacitance needed for impedance matching (Figure 5(c)). We consider two in-vivo endpoint locations, behind a fat layer 1 cm and 3 cm in thickness respectively, and measure 15 air-tissue links for each. RF-Mediator provides high RSSI gains similarly for the two in-vivo locations despite different amounts of fat involved (Figure 25). As in previous setups, a non-programmable surface achieves a median gain over 5 dB lower than RF-Mediator, highlighting the benefit of adapting to medium consistency.

F. Control Algorithm Microbenchmarks

Beamforming near-optimality. Recall that for beamforming in stage two of our algorithm, we adopt fine-grained, element-wise control but prune the search space. Therefore, we assess the benefit of the former and the cost of the latter. We experiment with three algorithm variants, each over 45 air-to-water links: (i) Brute-force column-wise control, enumerating all configurations of 8 columns, with 2^8 channel measurements; (ii) our algorithm applied to column-wise adaptation of 8 columns, with 32 measurements only; and (iii) the RF-Mediator default, element-wise control of 64 elements, with 128 measurements. The first variant provides the optimal result for 8 columns, while our 8-column algorithm exhibits near-optimal performance (Figure 26) but one-eighth the feedback measurements. Controlling 64 elements individually often provides extra gains of 2-3 dB compared to 8 columns, highlighting the benefit of element-wise control.

Voltage control effectiveness. We analyze the voltage values chosen in the first algorithm stage (Figure 27) to understand whether the control algorithm is operating as expected. The coupling between the surface and water affects the results with 1 mm gap due to the proximity, which is also observed in HFSS simulations. As the medium-interface gap increases from 2 mm to 9 mm, the median of the selected voltage increases from lower than 5V to 10V, indicating the corresponding varactor capacitance and surface admittance are decreasing. This descending trend agrees with our theoretical analysis and simulations results (Figure 5(a)).

G. Surface Flexibility

The flexibility of our single-layer metasurface facilitates practical deployment in various application scenarios by adapting the shape. For air-body networking especially, it can conform to the human body shape and ensures a good medium impedance matching performance over the whole covered region for a reliable air-to-body wireless connectivity. We demonstrate the benefit of surface flexibility with HFSS [68] simulations, as shown in Figure 28.

We simulate the 2D cross-section of a human body model [80], which includes multi-layer tissue shells and internal organs, with and without the metasurfaces. To compare the performance, we plot the signal power density distributions with plane waves illuminating the front of human body model. Without a metasurface, the baseline result shows a weak power in the stomach and intestine. When we deploy a rigid planar surface, we observe a higher power density in a small region where the surface is close to the air-body interface and resonates properly. When we deploy a flexible surface, the surface can conform to the shape of human body and maintain the proximity across the area covered by the surface. Though bent to a curved shape, our surface remains functional, enhancing the through-interface transmission and provides a stronger power density than the planar counterpart. We further demonstrate the extra enhancement of beamforming based on element-wise control. Assuming we want to focus energy towards the center of the human body, we adjust the surface element configuration to optimize the power density at the center using the procedure of our control algorithm. As shown in Figure 28, we see a stronger and more focused beam reaching the intestine in the center of body model.

Safety. Our metasurface minimizes reflection power loss without active amplification and performs beamforming with a compact size to combat path loss. We do not increase the received power beyond safety limits, only make it more efficient from the transmitter perspective. Figure 28 shows our surface does not concentrate energy excessively. As long as the active endpoints follow established exposure limits, our system should not pose additional safety risk.

VI. Discussion

We discuss future research directions to extend the application of tuning medium interfaces.

Security protection. Recent work [81], [82] investigate security issues of wireless sensing, as through-wall wireless

sensing challenges the perception of indoor privacy. Our surface can significantly reduce the reflection from human body, akin to invisible cloaks, or dynamically adjust the reflection to protect user privacy against unwanted sensing activities.

Sensing the medium composition. Our system adapts to different media via programmability; The reverse process can sense environmental information. Specifically, by observing the voltage that achieves medium impedance matching, we can extract information about the type and composition of the target medium by estimating its permittivity. For example, we can estimate glucose level by sensing the medium [83].

VII. Conclusion

Cross-medium wireless face the fundamental challenge of signal degradation when waves propagate through medium interfaces. In this paper, we present a lightweight programmable metasurface system, RF-Mediator, to tackle the root cause of the problem via novel device-protocol co-design. When placed at or near the medium interface, our transflective metasurface dynamically mediates the medium media, boosting connectivity for multiple endpoints on both sides of the surface simultaneously. Our prototype implementation on a single layer of thin and flexible plastic sheet is amenable to diverse applications. This provides an enabling technology for future IoT applications in challenging communication settings.

Acknowledgment

The work of Ruichun Ma was completed when he was with Yale University.

References

[1] R. Ma and W. Hu, "RF-mediator: Tuning medium interfaces with flexible metasurfaces," in *Proc. 30th Annu. Int. Conf. Mobile Comput. Netw.*, May 2024, pp. 155–169.

[2] Z. Yu et al., "Magnetoelectric backscatter communication for millimeter-sized wireless biomedical implants," in *Proc. 28th Annu. Int. Conf. Mobile Comput. Netw.* New York, NY, USA: Association for Computing Machinery, Oct. 2022, pp. 432–445.

[3] X. Fan et al., "Towards flexible wireless charging for medical implants using distributed antenna system," in *Proc. ACM MobiCom*. New York, NY, USA: Association for Computing Machinery, 2020, pp. 1–15.

[4] M. R. Abdelhamid, R. Chen, J. Cho, A. P. Chandrakasan, and F. Adib, "Self-reconfigurable micro-implants for cross-tissue wireless and batteryless connectivity," in *Proc. 26th Annu. Int. Conf. Mobile Comput. Netw.* New York, NY, USA: Association for Computing Machinery, Sep. 2020, pp. 1–14.

[5] D. Vasisht, G. Zhang, O. Abari, H.-M. Lu, J. Flanz, and D. Katabi, "In-body backscatter communication and localization," in *Proc. Conf. ACM Special Interest Group Data Commun.* New York, NY, USA: Association for Computing Machinery, Aug. 2018, pp. 132–146.

[6] Y. Ma, Z. Luo, C. Steiger, G. Traverso, and F. Adib, "Enabling deep-tissue networking for miniature medical devices," in *Proc. Conf. ACM Spec. Interest Group Data Commun.* New York, NY, USA: Association for Computing Machinery, 2018, pp. 417–431.

[7] V. Iyer, V. Talla, B. Kellogg, S. Gollakota, and J. R. Smith, "Inter-technology backscatter: Towards internet connectivity for implanted devices," in *Proc. ACM SIGCOMM Conf.* New York, NY, USA: Association for Computing Machinery, Jan. 2016, pp. 356–369.

[8] F. Tonolini and F. Adib, "Networking across boundaries: Enabling wireless communication through the water-air interface," in *Proc. Conf. ACM Special Interest Group Data Commun.* New York, NY, USA: Association for Computing Machinery, Aug. 2018, pp. 117–131.

[9] C. J. Carver, T. Zhao, H. Zhang, K. Odame, A. Q. Li, and X. Zhou, "AmphiLight: Direct air-water communication with laser light," in *Proc. 17th Usenix Conf. Networked Syst. Des. Implement.*, Jan. 2020, pp. 373–388.

[10] J. Ding and R. Chandra, "Towards low cost soil sensing using Wi-Fi," in *Proc. 25th Annu. Int. Conf. Mobile Comput. Netw.* New York, NY, USA: Association for Computing Machinery, Oct. 2019, pp. 1–16.

[11] U. M. Khan and M. Shahzad, "Estimating soil moisture using RF signals," in *Proc. 28th Annu. Int. Conf. Mobile Comput. Netw.* New York, NY, USA: Association for Computing Machinery, Oct. 2022, pp. 242–254.

[12] A. Burton et al., "Wireless, battery-free subdermally implantable photometry systems for chronic recording of neural dynamics," *Proc. Nat. Acad. Sci. USA*, vol. 117, no. 6, pp. 2835–2845, Feb. 2020.

[13] G. Traverso et al., "Physiologic status monitoring via the gastrointestinal tract," *PLoS ONE*, vol. 10, no. 11, Nov. 2015, Art. no. e0141666. [Online]. Available: https://journals.plos.org/plosone/article?id=10.1371/journal.pone.0141666

[14] S. Sharma et al., "Location-aware ingestible microdevices for wireless monitoring of gastrointestinal dynamics," *Nature Electron.*, vol. 6, no. 3, pp. 242–256, Feb. 2023.

[15] G. Iddan, G. Meron, A. Glukhovsky, and P. Swain, "Wireless capsule endoscopy," *Nature*, vol. 405, no. 6785, p. 417, 2000.

[16] C. H. Lee et al., "Biological lipid membranes for on-demand, wireless drug delivery from thin, bioresorbable electronic implants," *NPG Asia Mater.*, vol. 7, no. 11, p. e227, Nov. 2015. [Online]. Available: https://www.nature.com/articles/am2015114

[17] F. T. Sun and M. J. Morrell, "Closed-loop neurostimulation: The clinical experience," *Neurotherapeutics*, vol. 11, no. 3, pp. 553–563, Jul. 2014.

[18] N. M. Schuster and A. M. Rapoport, "New strategies for the treatment and prevention of primary headache disorders," *Nature Rev. Neurol.*, vol. 12, no. 11, pp. 635–650, Oct. 2016.

[19] *Tidal: Protecting the Ocean While Feeding Humanity Sustainably*. Accessed: Jun. 30, 2025. [Online]. Available: https://x.company/projects/tidal/

[20] S. S. Afzal et al., "Battery-free wireless imaging of underwater environments," *Nature Commun.*, vol. 13, no. 1, p. 5546, Sep. 2022.

[21] M. Ho, S. El-Borgi, D. Patil, and G. Song, "Inspection and monitoring systems subsea pipelines: A review paper," *Structural Health Monitor.*, vol. 19, no. 2, pp. 606–645, Mar. 2020.

[22] L. Bandyopadhyay, S. Chaulya, and P. Mishra, "*Wireless Communication in Underground Mines: RFID-based Sensor Networking*, vol. 22, 2010.

[23] K. A. Remley, G. Koepke, D. G. Camell, C. Grosvenor, G. Hough, and R. T. Johnk, "Wireless communications in tunnels for urban search and rescue robots," in *Proc. 8th Workshop Perform. Metrics Intell. Syst.* New York, NY, USA: Association for Computing Machinery, Aug. 2008, pp. 236–243.

[24] H. M. Jol, *Ground Penetrating Radar Theory and Applications*. Amsterdam, The Netherlands: Elsevier, Dec. 2008.

[25] J. Blauert and A. Kiourti, "Theoretical modeling and design guidelines for a new class of wearable bio-matched antennas," *IEEE Trans. Antennas Propag.*, vol. 68, no. 3, pp. 2040–2049, Mar. 2020.

[26] J. Blauert and A. Kiourti, "Bio-matched antennas with flare extensions for reduced low frequency cutoff," *IEEE Open J. Antennas Propag.*, vol. 1, pp. 136–141, 2020.

[27] D. R. Agrawal et al., "Conformal phased surfaces for wireless powering of bioelectronic microdevices," *Nature Biomed. Eng.*, vol. 1, no. 3, pp. 1–9, Mar. 2017. [Online]. Available: https://www.nature.com/articles/s41551-017-0043

[28] X. Guo, Y. He, Z. Yu, J. Zhang, Y. Liu, and L. Shangguan, "RF-transformer: A unified backscatter radio hardware abstraction," in *Proc. ACM MobiCom*, Oct. 2022, pp. 446–458.

[29] A. Welkie, L. Shangguan, J. Gummeson, W. Hu, and K. Jamieson, "Programmable radio environments for smart spaces," in *Proc. Workshop Hot Topics Netw. (HotNets)*, Nov. 2017, pp. 36–42.

[30] Z. Li et al., "Towards programming the radio environment with large arrays of inexpensive antennas," in *Proc. Symp. Networked Syst. Design Implement. (NSDI)*, Jan. 2019, pp. 285–300.

[31] L. Chen, W. Hu, K. Jamieson, X. Chen, D. Fang, and J. Gummeson, "Pushing the physical limits of IoT devices with programmable metasurfaces," in *Proc. Symp. Networked Syst. Design Implement. (NSDI)*, Jul. 2021, pp. 425–438.

[32] V. Arun and H. Balakrishnan, "RFocus: Practical beamforming for small devices," in *Proc. Symp. Networked Syst. Design Implement. (NSDI)*, Jan. 2020, pp. 1047–1061.

[33] M. Dunna, C. Zhang, D. Sievenpiper, and D. Bharadia, "ScatterMIMO: Enabling virtual MIMO with smart surfaces," in *Proc. 26th Annu. Int. Conf. Mobile Comput. Netw.*, 2020, pp. 1–14.

[34] C. Feng et al., "RFlens: Metasurface-enabled beamforming for IoT communication and sensing," in *Proc. 27th Annu. Int. Conf. Mobile Comput. Netw.* New York, NY, USA: Association for Computing Machinery, Oct. 2021, pp. 587–600.

[35] R. I. Zelaya, W. Sussman, J. Gummeson, K. Jamieson, and W. Hu, "LAVA: Fine-grained 3D indoor wireless coverage for small IoT devices," in *Proc. Conf. ACM Special Interest Group Data Commun. (SIGCOMM)*, 2021, pp. 123–136.

[36] R. I. Zelaya et al., "Towards 6G and beyond: Smarten everything with metamorphic surfaces," in *Proc. 20th ACM Workshop Hot Topics Netw. (HotNets)*, 2021, pp. 155–162.

[37] K. W. Cho, M. H. Mazaheri, J. Gummeson, O. Abari, and K. Jamieson, "mmWall: A steerable, transflective metamaterial surface for NextG mmWave networks," in *Proc. 20th USENIX Symp. Networked Syst. Design Implement. (NSDI)*, 2023, pp. 1647–1665.

[38] R. Ma, R. I. Zelaya, and W. Hu, "Softly, deftly, scrolls unfurl their splendor: Rolling flexible surfaces for wideband wireless," in *Proc. 29th Annu. Int. Conf. Mobile Comput. Netw.*, Jul. 2023, pp. 1–15.

[39] H. Pan et al., "PMSat: Optimizing passive metasurface for low Earth orbit satellite communication," in *Proc. 29th Annu. Int. Conf. Mobile Comput. Netw.*, Oct. 2023, pp. 1–15.

[40] R. Ma et al., "AutoMS: Automated service for mmWave coverage optimization using low-cost metasurfaces," in *Proc. 30th Annu. Int. Conf. Mobile Comput. Netw.*, May 2024, pp. 62–76.

[41] R. Ma, L. Qiu, and W. Hu, "SurfOS: Towards an operating system for programmable radio environments," in *Proc. 23rd ACM Workshop Hot Topics Netw.*, Nov. 2024, pp. 132–141.

[42] F. Yang, D. T. Nguyen, B. O. Raeker, A. Grbic, and J. S. Ho, "Near-reflectionless wireless transmission into the body with cascaded metasurfaces," *IEEE Trans. Antennas Propag.*, vol. 70, no. 9, pp. 8379–8388, Sep. 2022.

[43] F. Yang et al., "Antireflection and wavefront manipulation with cascaded metasurfaces," *Phys. Rev. Appl.*, vol. 14, no. 6, Dec. 2020, Art. no. 064044.

[44] D. Vasisht et al., "Farmbeats: An IoT platform for data-driven agriculture," in *Proc. USENIX NSDI*, 2017, pp. 515–529.

[45] D. M. Pozar, *Microwave Engineering*. Hoboken, NJ, USA: Wiley, 2011.

[46] C. Gabriel, S. Gabriel, and E. Corthout, "The dielectric properties of biological tissues: I. Literature survey," *Phys. Med. Biol.*, vol. 41, no. 11, p. 2231, 1996.

[47] D. Nikolayev, M. Zhadobov, P. Karban, and R. Sauleau, "Electromagnetic radiation efficiency of body-implanted devices," *Phys. Rev. Appl.*, vol. 9, no. 2, Feb. 2018, Art. no. 024033.

[48] Z. Gong, Z. An, D. Dai, J. Tong, S. H. Long, and L. Yang, "Enabling cross-medium wireless networks with miniature mechanical antennas," in *Proc. 30th Annu. Int. Conf. Mobile Comput. Netw.*, May 2024, pp. 648–662.

[49] S. Genovesi, I. R. Butterworth, J. E. C. Serrallés, and L. Daniel, "Metasurface matching layers for enhanced electric field penetration into the human body," *IEEE Access*, vol. 8, pp. 197745–197756, 2020.

[50] A. H. Dorrah, M. Chen, and G. V. Eleftheriades, "Bianisotropic huygens' metasurface for wideband impedance matching between two dielectric media," *IEEE Trans. Antennas Propag.*, vol. 66, no. 9, pp. 4729–4742, Sep. 2018.

[51] H. Cano-García, P. Kosmas, and E. Kallos, "Enhancing electromagnetic transmission through biological tissues at millimeter waves using subwavelength metamaterial antireflection coatings," in *Proc. 9th Int. Congr. Adv. Electromagn. Mater. Microw. Opt. (METAMATERIALS)*, Sep. 2015, pp. 43–45.

[52] T. Hao, W. Zheng, W. He, and K. Lin, "Air-ground impedance matching by depositing metasurfaces for enhanced GPR detection," *IEEE Trans. Geosci. Remote Sens.*, vol. 58, no. 6, pp. 4061–4075, Jun. 2020.

[53] J. Nolan, B. Chen, and X. Zhang, "MetaLink: Extending air-to-water wireless communications using passive bianisotropic metasurfaces," *Proc. 22nd ACM Conf. Embedded Networked Sensor Syst.*, pp. 155–168, Nov. 2024.

[54] H. Zhang and B. Di, "Intelligent omni-surfaces: Simultaneous refraction and reflection for full-dimensional wireless communications," *IEEE Commun. Surveys Tuts.*, vol. 24, no. 4, pp. 1997–2028, 4th Quart., 2022.

[55] H. Zhang et al., "Intelligent omni-surfaces for full-dimensional wireless communications: Principles, technology, and implementation," *IEEE Commun. Mag.*, vol. 60, no. 2, pp. 39–45, Feb. 2022.

[56] X. Tian et al., "Implant-to-implant wireless networking with metamaterial textiles," *Nat. Commun.*, vol. 14, no. 1, p. 4335, 2023.

[57] E. Bok, J. J. Park, H. Choi, C. K. Han, O. B. Wright, and S. H. Lee, "Metasurface for water-to-air sound transmission," *Phys. Rev. Lett.*, vol. 120, no. 4, Jan. 2018, Art. no. 044302.

[58] Z. Huang et al., "Tunable fluid-type metasurface for wide-angle and multifrequency water-air acoustic transmission," in *Research*, vol. 2021, Jan. 2021.

[59] J.-J. Liu, Z.-W. Li, B. Liang, J.-C. Cheng, and A. Alu, "Remote water-to-air eavesdropping through phase-engineered impedance matching metasurfaces," 2022, *arXiv:2208.12999*.

[60] C. Pfeiffer and A. Grbic, "Metamaterial Huygens' surfaces: Tailoring wave fronts with reflectionless sheets," *Phys. Rev. Lett.*, vol. 110, no. 19, May 2013, Art. no. 197401.

[61] C. Pfeiffer and A. Grbic, "Cascaded metasurfaces for complete phase and polarization control," *Appl. Phys. Lett.*, vol. 102, no. 23, Jun. 2013, Art. no. 231116.

[62] P. Zhang, M. Rostami, P. Hu, and D. Ganesan, "Enabling practical backscatter communication for on-body sensors," in *Proc. ACM SIGCOMM Conf.* New York, NY, USA: Association for Computing Machinery, Aug. 2016, pp. 370–383.

[63] D. Bharadia, K. R. Joshi, M. Kotaru, and S. Katti, "BackFi: High throughput WiFi backscatter," in *Proc. ACM SIGCOMM Comput. Commun. Rev.*, 2015, vol. 45, no. 4, pp. 283–296.

[64] Z. Wu, Y. Ra'di, and A. Grbic, "Tunable metasurfaces: A polarization rotator design," *Phys. Rev. X*, vol. 9, no. 1, Feb. 2019, Art. no. 011036.

[65] Z. Wu, C. Scarborough, and A. Grbic, "Space-time-modulated metasurfaces with spatial discretization: Free-space n-path systems," *Phys. Rev. Appl.*, vol. 14, no. 6, Dec. 2020, Art. no. 064060.

[66] *SMV1405: Plastic Packaged Abrupt Junction Tuning Varactors*. Accessed: Jun. 30, 2025. [Online]. Available: https://www.mouser.com/datasheet/2/472/200068N-15249.pdf

[67] *SPICE (Simulation Program With Integrated Circuit Emphasis)*. Accessed: Jun. 30, 2025. [Online]. Available: https://en.wikipedia.org/wiki/SPICE

[68] *Ansys HFSS 3D High Frequency Simulation Software*. Accessed: Jun. 30, 2025. [Online]. Available: https://www.ansys.com/products/electronics/ansys-hfss

[69] *MPC4728: 12-Bit, Quad Digital-to-Analog Converter*. Accessed: Jun. 30, 2025. [Online]. Available: http://ww1.microchip.com/downloads/en/devicedoc/22187e.pdf

[70] *LM358: Dual Operational Amplifier*. Accessed: Jun. 30, 2025. [Online]. Available: https://www.ti.com/lit/ds/symlink/lm358.pdf

[71] *Epressif ESP32-DevKitC Board*. Accessed: Jun. 30, 2025. [Online]. Available: https://www.espressif.com/en/products/devkits/esp32-devkitc

[72] *CD405xB CMOS Single 8-Channel Analog Multiplexer or Demultiplexer*. Accessed: Jun. 30, 2025. [Online]. Available: https://www.ti.com/lit/ds/symlink/cd4053b.pdf

[73] L. M. Thring, D. Boddice, N. Metje, G. Curioni, D. N. Chapman, and L. Pring, "Factors affecting soil permittivity and proposals to obtain gravimetric water content from time domain reflectometry measurements," *Can. Geotechnical J.*, vol. 51, no. 11, pp. 1303–1317, Nov. 2014.

[74] Y. Yamada, "Dielectric properties of textile materials: Analytical approximations and experimental measurements—A review," *Textiles*, vol. 2, no. 1, pp. 50–80, Jan. 2022. [Online]. Available: https://www.mdpi.com/2673-7248/2/1/4

[75] *Dielectrical Constants of Polymers*. Accessed: Jun. 30, 2025. [Online]. Available: https://polymerdatabase.com/polymer%20physics/Epsilon%20Table.html

[76] *Ettus Research USRP N210*. Accessed: Jun. 30, 2025. [Online]. Available: https://www.ettus.com/all-products/un210-kit/

[77] *Alpha Network Antenna APA-M25*. Accessed: Jun. 30, 2025. [Online]. Available: https://www.alfa.com.tw/products_detail/234.htm

[78] *LairdConnect FlexNotch WiFi and Bluetooth Flexible 2.4 GHz Antenna*. Accessed: Jun. 30, 2025. [Online]. Available: https://www.lairdconnect.com/RF-antennas/wifi-antennas/internal-antennas/flexnotch-24-ghz-antenna

[79] *MAST Technologies Lossy Foam Absorber*. Accessed: Jun. 30, 2025. [Online]. Available: https://www.masttechnologies.com/products/commercial/RF-absorbers-commercial/lossy-foam-0-5/

[80] S. N. Makarov et al., "Virtual human models for electromagnetic studies and their applications," *IEEE Rev. Biomed. Eng.*, vol. 10, pp. 95–121, 2017.

[81] J. Shenoy, Z. Liu, B. Tao, Z. Kabelac, and D. Vasisht, "RF-protect: Privacy against device-free human tracking," in *Proc. ACM SIGCOMM Conf.*, 2022, pp. 588–600.

[82] A. Abedi and D. Vasisht, "Non-cooperative Wi-Fi localization & its privacy implications," in *Proc. 28th Annu. Int. Conf. Mobile Comput. Netw.* New York, NY, USA: Association for Computing Machinery, Oct. 2022, pp. 570–582.

[83] H. Pan et al., "CGMM: Non-invasive continuous glucose monitoring in wearables using metasurfaces," in *Proc. 31st Annu. Int. Conf. Mobile Comput. Netw.*, 2025, pp. 1–15.